Journal of Alloys and Compounds xxx (xxxx) xxx

Contents lists available at ScienceDirect

Journal of Alloys and Compounds

journal homepage: http://www.elsevier.com/locate/jalcom

# Enhanced thermal stability of exciton recombination in $CsPbI_3$ perovskite nanocrystals via zinc alloying

Ruirui Wu [a], Qi Wang [a], Sen Yang [a], Lifang Wu [a], Shunfa Gong [a], Qiuju Han [b], Wenzhi Wu [a], *

[a] School of Electronic Engineering, Heilongjiang University, Harbin, Heilongjiang, 150080, China
[b] School of College of Arts and Sciences, Northeast Agricultural University, Harbin, Heilongjiang, 150030, China

## ARTICLE INFO

*Article history:*
Received 14 August 2020
Received in revised form
25 September 2020
Accepted 12 October 2020
Available online xxx

*Keywords:*
$CsPb_{1-x}Zn_xI_3$ PNCs
Exciton recombination
Temperature dependence
Exciton binding energy
Excited state

## ABSTRACT

In this work, the $Pb^{2+}$ substitution with $Zn^{2+}$ in $CsPbI_3$ perovskite nanocrystals (PNCs) is partially achieved to improve the optoelectronic properties through temperature-pressure assisted crystallization approach. The spectral and dynamic exciton recombination for zinc alloyed $CsPbI_3$ PNCs are probed with steady-state/time-resolved PL (TRPL), transient absorption (TA) techniques. Compared with pure $CsPbI_3$ PNCs, PLQY can be boosted to 60% when incorporating the optimal amount of $ZnI_2$ in the synthesis, and long-term thermal stability are obtained in a series of red-emitting alloyed $CsPbI_3$ PNCs. Simultaneously, the change of exciton binding energy and average optical phonon energy indicate that weaker non-radiative transition for exciton recombination of zinc alloyed $CsPbI_3$ PNCs than those of $CsPbI_3$ PNCs. TRPL and TA spectroscopy are used to understand the photoinduced carrier relaxation processes. The carrier dynamics reveal that the coupling between Zn-induced lowest excited state and exciton trapping state is promoted in zinc alloyed $CsPbI_3$ PNCs, which can significantly enhance the efficiency of excitonic recombination. The improved performance of PLQY and thermal stability makes these zinc alloyed $CsPbI_3$ PNCs as appropriate perovskite materials for efficient optoelectronic devices.

## 1. Introduction

Inorganic metal halide perovskite nanocrystals (PNCs) with a chemical formula of $ABX_3$ (A=Cs; B=Pb; X=Cl, Br, or I) have made great breakthroughs in high-efficiency photoluminescence (PL), narrow bandwidth and tunable emission [1]. Taking into account these excellent properties, many researchers have taken these advantages for using in photovoltaic cells [2], photodetectors [3], lasers [4], and light-emitting diodes (LEDs) [5]. Nevertheless, their poor stability at thermal conditions greatly limits their practical applications, which is especially more obvious for $CsPbI_3$ PNCs among the all-inorganic Pb-based halide perovskite [6]. $CsPbI_3$ PNCs is a particularly promising candidate for solar cells [7] owing to its suitable optical bandgap (1.73 eV), though it has an inherent phase and chemical instability [8]. There are several reports to improve the stability of the perovskite by chemical treatment, surface coating or passivation [9,10]. Unlike $CsPbCl_3$ and $CsPbBr_3$[49], the functional cubic (α) phase for $CsPbI_3$ is stable at temperature below 315 °C. The metastable cubic-phase $CsPbI_3$ PNCs spontaneously transforms into the non-functional orthorhombic (δ) phase, also known as the "yellow phase", at room temperature preventing it from being effectively studied and harnessed in practical applications [11]. What calls for special attention is that the existence of defects in perovskite is still an important application problem, which cannot be ignored because these defects will reduce carrier injection efficiency and radiation recombination probability. The main reasons for the poor optical properties and low stability of $CsPbI_3$ PNCs are iodide deficiency associated point defects on the surface and distortion of the $[PbI_6]^{4-}$ octahedral units [12]. The thermal stability of pure $CsPbI_3$ PNCs is investigated extensively through temperature-dependent PL, which shows the distinct mechanisms on exciton recombination versus bulk materials [13].

The incorporation of some judiciously selected foreign ions is an effective method to change the structure of $CsPbI_3$ PNCs and this has recently attracted widespread attention [14]. For example, the $CH(NH_2)_2^+$ or $CH_3NH_3^+$ ions are the most well-known organic cations to replace the $Cs^+$, which give rise to an increase in tolerance factor

---

* Corresponding author.
*E-mail address:* wuwenzhi@hlju.edu.cn (W. Wu).

https://doi.org/10.1016/j.jallcom.2020.157574
0925-8388/© 2020 Elsevier B.V. All rights reserved.

Please cite this article as: R. Wu, Q. Wang, S. Yang *et al.*, Enhanced thermal stability of exciton recombination in $CsPbI_3$ perovskite nanocrystals via zinc alloying, Journal of Alloys and Compounds, https://doi.org/10.1016/j.jallcom.2020.157574

($t$). The black phase of $CsPbI_3$ PNCs ($t$=0.89−1.00) exhibits an undesirable tolerance factor that leads to poor phase stability, when exposed to ambient conditions. Consequently, the substitution of $Pb^{2+}$ cation is one of the promising methods for improving perovskite stability and reducing toxicity. To find a non-toxic element to replace toxic $Pb^{2+}$ for improved stability has been a common goal for researchers. Selectively, the influence of lead in $CsPbI_3$ PNCs on the environment can also be weakened. Sectional researchers are trying to completely replace lead with nontoxic elements such as Bi, Sb, Sn, Ti, Ca [15,16]. Reports on the addition of ruthenium caused an increase in surface defects and bandgap density of states, so that strong quenching of the PL is detrimental to the optoelectronic efficiency of the materials [17]. Compared with lead-containing perovskites, equipment performance of unstable lead-free perovskite results in a decline under environmental conditions due to the high defect density [18]. Besides, the quantum efficiency of lead-free perovskites is generally low and PLQY is not high. For example, the quantum efficiency of $CsSnBr_3$ PNCs is only 0.14% [19]. In the field of efficient optoelectronics, quantum efficiencies, PLQY of lead-free perovskites are far from enough compared with pure lead-based perovskites [20]. Zn incorporation has been identified $CsPbX_3$ PNCs with $ZnX_2$ to enhance its stability and PLQY [21].

In this work, we adopt an effective approach to improve the emission efficiency and thermal stability of $CsPbI_3$ PNCs by in-situ alloying Zn ions during the crystallization process. With increasing the ratio of alloyed $Zn^{2+}$ in $CsPbI_3$ PNCs, $Zn^{2+}$ can partly replace the $Pb^{2+}$ causing a slight lattice contraction . The PL dynamics of $CsPbI_3$ hosts are accordingly modulated due to the existence of alloying-induced near band-edge state, thereby leading to the enhancement of PLQY for $CsPbI_3$ PNCs. The pertinent mechanisms are revealed employing temperature-dependent TRPL and TA. It is confirmed that Zn incorporation in PNCs can suppress effectively the defect state. Consequently, PLQY and thermal stability of zinc alloyed $CsPbI_3$ PNCs are enhanced to an order of magnitude compared with pure $CsPbI_3$ PNCs.

## 2. Experimental

### 2.1. Materials

Lead iodide ($PbI_2$, 99%, Macklin), Cesium acetate (CsOAc, 99%, Aladdin), Zinc iodide ($ZnI_2$, 99%, Macklin), 1-octadecene (ODE, 95%, Macklin), Oleic acid (OA, 99%, Macklin), Oleylamine (OAm, 95%, Macklin), *n*-hexane (99%, Macklin).

### 2.2. Preparation of $CsPb_{1-x}Zn_xI_3$ (x=0.49, 0.36, 0.27, 0.12, 0) PNCs

A series of $CsPb_xZn_{1-x}I_3$ PNCs are synthesized according to temperature-pressure assisted crystallization method [22]. CsOAc (0.1 mmol, 0.02 g), $PbI_2$ (0.094, 0.118, 0.135, 0.162, 0.184 g), $ZnI_2$ (0.0625, 0.046, 0.034, 0.015, 0g) for $CsPb_{0.51}Zn_{0.49}I_3$, $CsPb_{0.64}Zn_{0.36}I_3$, $CsPb_{0.73}Zn_{0.27}I_3$, $CsPb_{0.88}Zn_{0.12}I_3$, $CsPbI_3$ PNCs are dissolved in ODE (15 mL), OA (1 mL), OAm (1 mL) with magnetic stirring at about 130 °C for 10 min. During our experiment of this method, instead of adding trioctylphosphine (TOP) and trioctylphosphine oxide (TOPO), the temperature is increased to facilitate the dissolution of $PbI_2$. The solution is then transferred into a Teflon-lined autoclave (25 mL) and kept at 160 °C in oven for 40 min. After the reaction solution is cooled down to room temperature, 10 mL of hexane is added to the solution, and the products are collected by centrifugation at speed of 10,000 rpm for 5 min. The precipitates are redispersed in 10 mL hexane and then centrifuged at 5000 rpm for 5 min. Due to relatively low reaction temperature and long reaction time without nitrogen protection, it is simpler and more efficient than hot injection method.

### 2.3. Steady-state PL spectroscopy and nanosecond TRPL spectroscopy

The emission and scattered light of the sample in the vertical direction of the laser is collected by a spectrometer (iHR550, Horiba) and detected by a charge-coupled device. A continuous-wave laser (MLL-III, CNI) at 405 nm is used as a light source for steady-state laser excitation. The temperature-dependent steady-state measurements are performed with temperature variations in the range of 80−310 K. Time-correlated single-photon counting (TCSPC, Boston Electronics) provides detailed information about the dynamics with the time resolution of 96 ps. The system consists of a monochromator (SSM101, Zolix) equipped with a detector (id100-50, ID Quantique) and a single-photon counting electronic module (SPC-130, Becker & Hickl GmbH) accounting for data acquisition. A supercontinuum picosecond laser (Surperk Extreme EXB-4, NKT Photonics) chosen the wavelength at 450 nm is used to excite the samples.

### 2.4. Transient absorption spectroscopy

Laser pluses at 800 nm are focused onto a sapphire window with a thickness of 2 mm to produce white continuum light extending from 380 to 800 nm, which is divided into the probe beam and the reference beam. Detection of probe pulses is done with and without pump using a 500 Hz mechanical chopper. A pump beam at 400 nm is used in all the TA measurements. Two highly sensitive spectrometers (Avantes-950F, Avantes) are used to collect the probe and reference beams for recording and calculating TA dynamics. The relative delay between the pump and probe pulse is controlled with the help of a stepper motor-driven optical delay line (TSA-200, Zolix).

## 3. Results and discussion

### 3.1. Characterization of the $CsPb_{1-x}Zn_xI_3$ PNCs

In our cases, it is important to note that x/(1-x) refers to the feed ratio of $ZnI_2/PbI_2$. The synthesis procedures of zinc alloyed $CsPbI_3$ PNCs are illustrated in Fig. 1(a). Consequently, five samples with different x are synthesized by changing the ratio of $ZnI_2$ and $PbI_2$ in the precursors. Fig. 1(b) presents the photographs of $CsPb_{1-x}Zn_xI_3$ PNCs in hexane under daylight and UV lamp irradiation. Their emission intensity increases at first and then decreases with the increasing concentration of Zn alloying. Accordingly, the PL intensity of zinc alloyed $CsPbI_3$ PNCs are enhanced, which indicates the relaxation pathway of highly efficient electron-hole recombination exists. The PL peak of the PNCs has a regular shift to the blue with increasing $Zn^{2+}$ content in $CsPbI_3$ PNCs hosts, the absorption peaks show no appreciable changes in location as shown in Fig. 1 (c). Simultaneously, the PL peak varies from 690 to 688, 685, 683, and 682 nm as x varies from 0 to 0.12, 0.27, 0.36, and 0.49, respectively. Generally, the blue-shifted PL spectra can be attributed to the contraction of the host perovskite, leading to a stronger interaction between Pb and I orbitals. This octahedral contraction leads to higher formation energy of Zn−I bond than that of Pb−I bond, which further leads to more stable lattice and greatly improves thermal stability [23]. To verify the incorporation of guest $Zn^{2+}$ ions, we measure the chemical composition of $CsPb_{0.64}Zn_{0.36}I_3$ PNCs by the energy-dispersive X-ray spectroscopy (EDX). In addition to the elements of Cs, Pb, and I, Zn is also identified in PNCs as shown in Fig. 1 (d). Moreover, the analysis of EDX spectrum gives a quantified atom ratio (%) of 36.4:3.5:57.3:2.8 for Cs/Pb/I/Zn. A relatively high Zn volume indicates that $Zn^{2+}$ ions are effectively alloyed in the hosts of $CsPbI_3$ PNCs. Cs-rich form in PNCs is expected

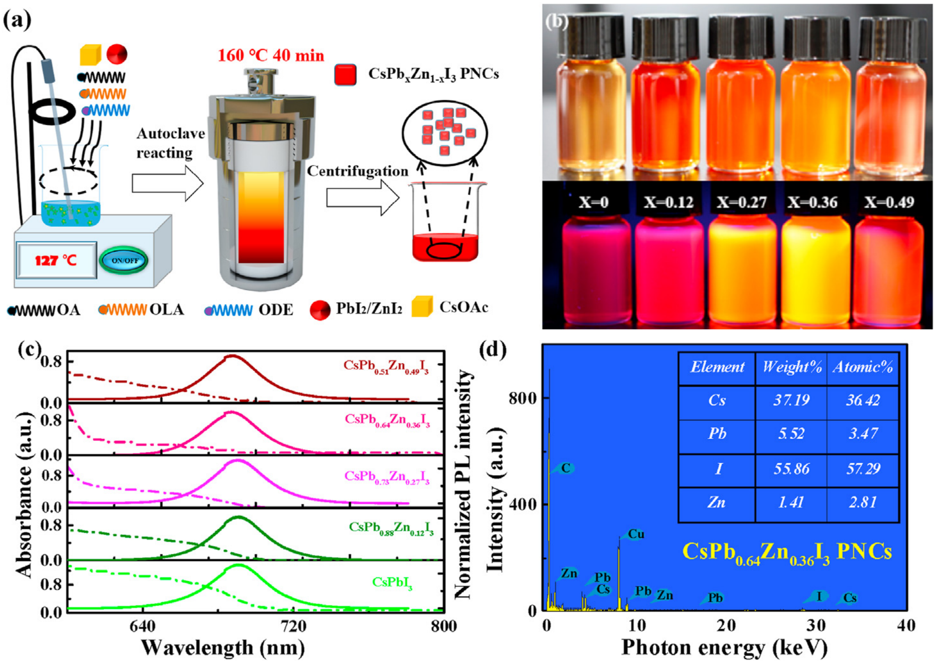

**Fig. 1.** (a) Schematic illustration of the process to fabricate CsPb$_{1-x}$Zn$_x$I$_3$ PNCs. (b) The corresponding colloidal samples under daylight and UV light (365 nm) lamp. (c) Absorption and PL spectra of pure CsPbI$_3$ and CsPb$_{1-x}$Zn$_x$I$_3$ PNCs. (d) EDX spectrum of as-synthesized CsPb$_{0.64}$Zn$_{0.36}$I$_3$ PNCs, inset is the list of element analysis for CsPb$_{0.64}$Zn$_{0.36}$I$_3$ PNCs.

to confirm the existence of a new surface of the perovskite with enhanced structural stability [24].

Transmission electron microscopy (TEM) images display PNCs morphology and size distribution of CsPb$_{1-x}$Zn$_x$I$_3$ PNCs as shown in Fig. 2(a–f). The typical TEM images of CsPb$_{1-x}$Zn$_x$I$_3$ PNCs (others x values as shown in Fig. S1) express a batch of NCs forming a cubic morphology and distributing densely. As shown in insets of Fig. 2, when x increases, normal distribution histograms demonstrate that average diameters of PNCs, are 14.4±1.6, 14.6 ±1.4, 13.7±2.6, 10.9±1.3, and 10.6±2.2 nm, respectively. The decrease in particle size at high Zn content may be attributed to the increased uptake of iodide ions, which inhibit the further growth of PNCs [25]. High-resolution TEM (HRTEM) images in top right insets of Fig. 2 (b, d) show that the lattice constants decrease from 5.8 Å to 5.7 Å as the x

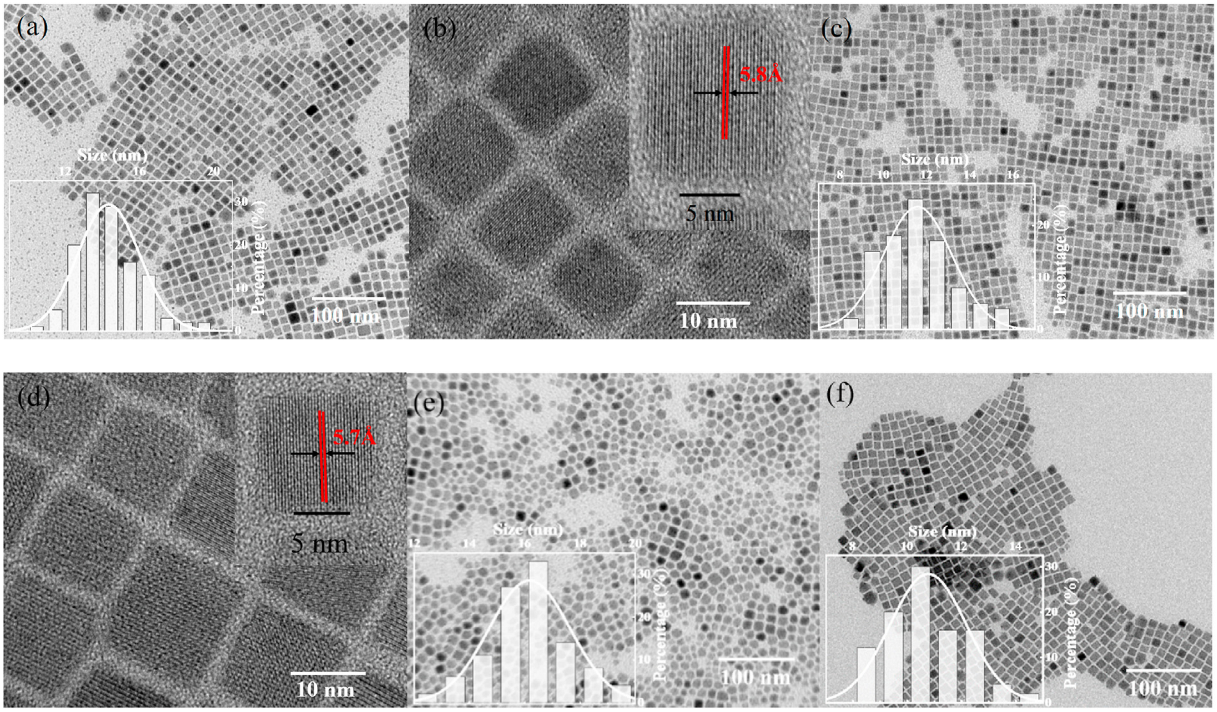

**Fig. 2.** TEM and HRTEM images of PNCs with x=0 (a, b); 0.36 (c, d); The size distributions are also included. TEM images of PNCs after one month for x=0 (e); 0.36 (f).

value increases from 0 to 0.49. It is in a good agreement with the lattice contraction owing to the larger Pb ions substituted with the smaller Zn ions. Considering the influence of zinc alloying on the stability of $CsPbI_3$ PNCs, the samples are preserved in dark at 4 °C after 30 days and then TEM images are tested as shown in Fig. 2 (e, f). Obviously, cubic structure of $CsPbI_3$ PNCs disappears, spherical particles appear after 30 days, which indicates the degradation of PNCs attributed to thermal effect [26]. In contrast, $CsPb_{0.64}Zn_{0.36}I_3$ PNCs basically remain original lattice structure after 30 days. The size distribution calculation is performed for these two samples as shown in insets of Fig. 2 (e, f). The size of $CsPbI_3$ PNCs increases from 14.4 nm to 16.5 nm, while that of $CsPb_{0.64}Zn_{0.36}I_3$ PNCs hardly changes. This is because of the intrinsic instability of the pure α-phase $CsPbI_3$ PNCs, which transform into the δ-phase and lost the desired optoelectronic properties.

### 3.2. *Temperature-dependent steady-state PL*

Temperature-dependent PL measurements are performed for a series of samples within the temperature range of 80–310 K. As seen in Fig. 3 (a, b), temperature-dependent PL spectra of pure $CsPbI_3$ and $CsPb_{0.64}Zn_{0.36}I_3$ PNCs are comparatively revealed, other samples are shown in Figs. S2 and S3, clear evolutions of peak position and intensity are also revealed. It is found that the PL spectral peak is blue-shifted with increasing temperature. This tendency is contrary to traditional Cd-based semiconductors, this atypical change is caused by the reverse band structure of perovskite [27]. It may also be related to the light-dark energy level inversion caused by Rashba effect suppressed by the enhanced electron-hole exchange interaction in NCs [28]. The PL intensity of $CsPb_{1-x}Zn_xI_3$ PNCs decreases gradually with the increase of temperature, which results from the thermally activated nonradiative recombination [29]. The normalized PL intensity of PNCs decreases with rising temperature as plotted in Fig. 3 (c). The experimental data can be fitted [30] by

$$I(T) = \frac{I_0}{1 + Ae^{-E_b/k_bT}} \tag{1}$$

where $I(T)$ and $I_0$ are the integrated PL intensity at temperature $T$ and 0 K, respectively, $A$ is a fitting parameter, $E_b$ is the exciton binding energy, and $k_b$ is the Boltzmann constant. As can be seen from in Fig. 3 (c), $E_b$ of $CsPbI_3$ PNCs is determined to be 51.2 meV. It is larger than that value calculated for those synthesized in hot-injection method [31], of which smaller sizes have a larger $E_b$ can be also consistent with the tendency reported [32]. Here, $E_b$ of $CsPb_{0.64}Zn_{0.36}I_3$ PNCs is 96.0 meV, which is nearly two times compared with that of pure $CsPbI_3$ PNCs, which is conducive to promote the radiative recombination [33]. The relatively higher $E_b$ ensures the survival of exciton well above room or even higher temperature with their high-rate recombination. Here, Zn alloying obviously improves exciton binding energy of $CsPb_{1-x}Zn_xI_3$ PNCs as shown in Fig. S4. The lattice structure due to Zn alloying compensates for the volume expansion under light radiation or higher temperature [34], and thus it may lead to improving stability dramatically for zinc alloyed $CsPbI_3$ PNCs.

The PL linewidth broadening in the temperature-dependent experiments are employed to analyze the phonon scattering in semiconductor materials. Fig. 3 (d) shows FWHM of $CsPbI_3$ PNCs and $CsPb_{0.64}Zn_{0.36}I_3$ PNCs as a function of temperature, which can be expressed as [35].

$$\Gamma(T) = \Gamma_0 + \sigma T + \Gamma_{\text{op}} \Big/ \left(e^{\hbar\omega_{op}/k_bT} - 1\right) \tag{2}$$

where $\Gamma(T)$ is the FWHM at temperature $T$, and $\Gamma_0$ is the inhomogeneous broadening contribution at 0 K, which is determined by material size, shape and composition [36]. $\sigma T$ is the homogeneous broadening term, which is ascribed to the acoustic phonon scattering through the deformation potential with exciton-acoustic phonon interaction strength of $\sigma$. $\Gamma_{op}$ is the exciton-optical

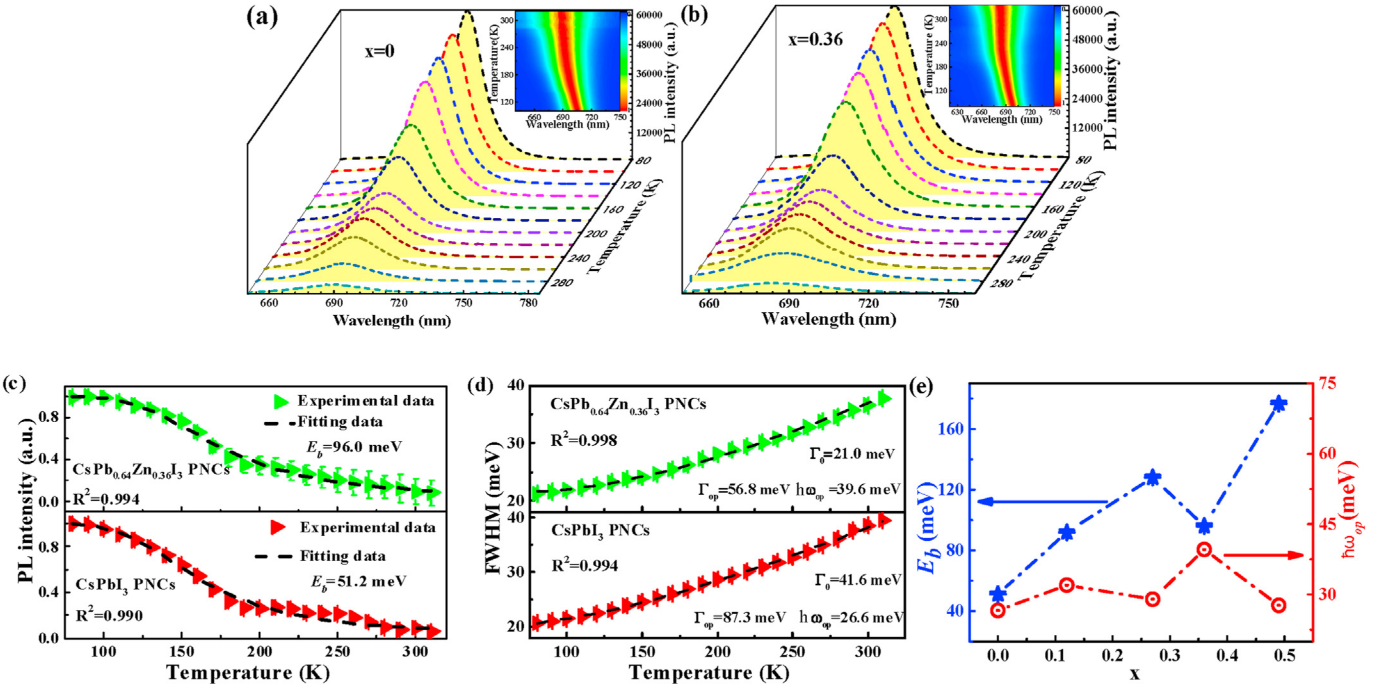

**Fig. 3.** Waterfall maps of temperature-dependent PL spectra of (a) $CsPbI_3$ and (b) $CsPb_{0.64}Zn_{0.36}I_3$ PNCs. Insets are the 2D color maps of temperature-dependent PL spectra. (c) Integrated PL intensity and (d) FWHM as a function of temperature. (e) $E_b$ and $\hbar\omega_{op}$as a function of x. (For interpretation of the references to color in this figure legend, the reader is referred to the Web version of this article.)

phonon contribution to the linewidth broadening, $\hbar\omega_{op}$is longitudinal opticalphonon energy. The first term $\Gamma_0$ dominates in Equation (2) at low temperature. The fitting results are shown in Fig. 3(d),$\hbar\omega_{op}$ involved in the exciton recombination is determined to be 39.6 meV, confirming strong exciton-phonon interaction and weak nonradiative transition for exciton recombination. The exciton binding energy as function of x in $CsPb_{1-x}Zn_xI_3$ PNCs are summarized in Fig. 3 (e). The value of longitudinal optical-phonon energy gets a maximum in $CsPb_{0.64}Zn_{0.36}I_3$ PNCs, which reveals that scattering centers with less exciton nonradiative relaxation.

### 3.3. *Environmental thermal stability of $CsPb_{1-x}Zn_xI_3$ PNCs*

To assess the long-term stability of $CsPb_{1-x}Zn_xI_3$ PNCs for practical optoelectronic device applications, we investigate the environmental thermal stability of the samples alternately by monitoring of PLQY and optical absorption within one month. Experimentally, the measurement of PLQY in detail is discussed in supporting information part VI. As shown in Fig. 4(a), the pristine $CsPbI_3$ PNCs experience a rapid PL quenching, PLQY retains only 5% after monitoring for 12 days. In sharp contrast, PLQY of $CsPb_{1-x}Zn_xI_3$ PNCs maintain high values and long-term stability. The PLQY increase from 6.9 to 27.7, 33.5, and 54.6% when x varies from 0 to 0.12 and 0.27 and 0.36 and then decrease to 13.8% when x further increases to 0.49. Though the values of PLQY synthesized with temperature-pressure assisted crystallization method are little smaller than that of similar zinc alloyed $CsPbI_3$ PNCs synthesized in hot-injection method [37], the simpler synthesis method and long-term stability are demonstrated. Among them, $CsPb_{0.64}Zn_{0.36}I_3$ PNCs exhibit optimized performance, of which initial and average value of PLQYs are 54.6 and 43.7% within one month, which shows that x = 0.36 is the optimal alloying amount. It can be seen from the previous literature that the incorporation of zinc ions increases the tolerance factor *t*, which is often used to assess the stability of the perovskite structure [38]. Fig. 4 (b, c) present the absorption spectra at different time intervals of $CsPbI_3$ and $CsPb_{0.64}Zn_{0.36}I_3$ PNCs. For pure $CsPbI_3$ PNCs, the gradual disappearance of absorption edges at ~700 nm is observed, and then the increased intensity of the absorbance appears at ~370 nm, which is caused by assigned to the phase transformation from cubic to orthorhombic [39]. After 15 days, we can observe that the absorption spectra for $CsPbI_3$ PNCs change dramatically, however, the absorption of $CsPb_{0.64}Zn_{0.36}I_3$ PNCs remain basically unchanged until after 30 days. The PL spectra have a redshift of 11.1, 4.8, 3.6, 1.1, 4.1 nm, when the x varies from 0 to 0.49. For the sake of further understand the influence of zinc alloying of host PNCs on the stability as shown in Fig. 2 (e) and (f), $CsPbI_3$ and $CsPb_{0.64}Zn_{0.36}I_3$ PNCs placed for one month are tested by TEM. Distinctly, pure $CsPbI_3$ PNCs is no longer as cubic morphology, while $CsPb_{0.64}Zn_{0.36}I_3$ PNCs remain basically unchanged. This improvement in both absorption spectrum and PL stability with Zn alloying agrees with our inference that the addition of $ZnI_2$ during postsynthesis alloying hinders the detrimental increase in PNCs size and thereby suppressing the conversion of cubic to orthorhombic phase.

### 3.4. *Temperature-dependent TRPL*

In order to clarify the band-edge PL dynamics, we therefore resort to TRPL measurements based on time-correlated single-photon counting. The PL decays of the samples are not single-exponential as seen in Fig. 5, indicating the existence of several emission centers in the PNCs. The normalized PL curves can be fitted by biexponential decay with convolution expressed [40] as

$$I(t) = A + \int_0^t \left(Be^{-(t-t')/\tau_1} + Ce^{-(t-t')/\tau_2}\right) e^{-\left(t'/\tau_{fwhm}\right)} dt' \qquad (3)$$

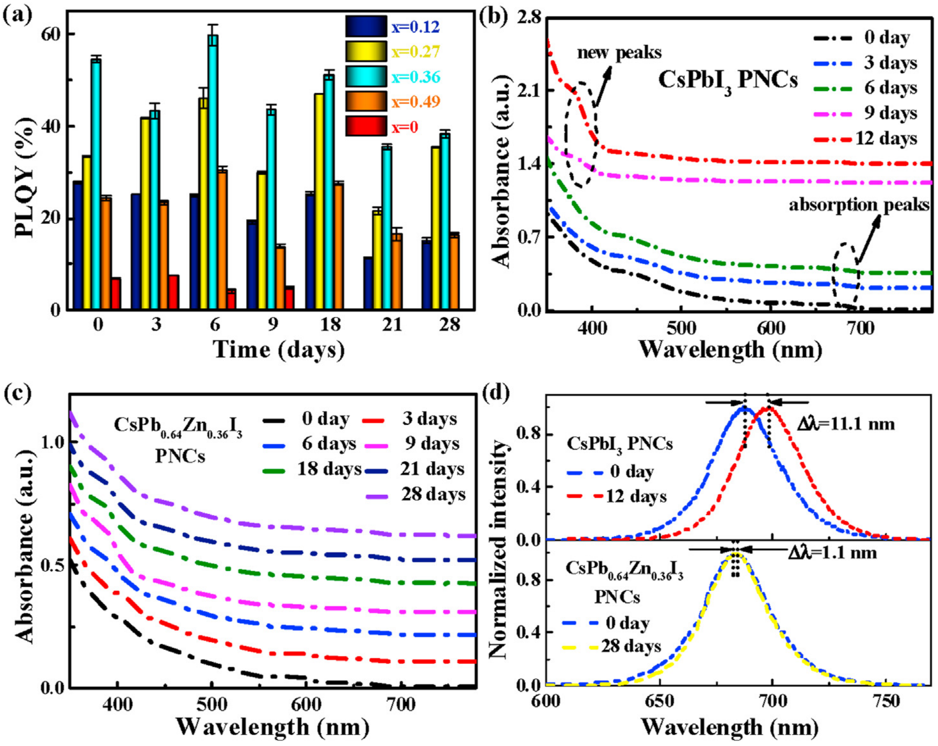

**Fig. 4.** (a) PLQY values, (b, c) absorption spectra, and (d) PL spectra as a function of aged days for $CsPb_{1-x}Zn_xI_3$ PNCs (x = 0, 0.36).

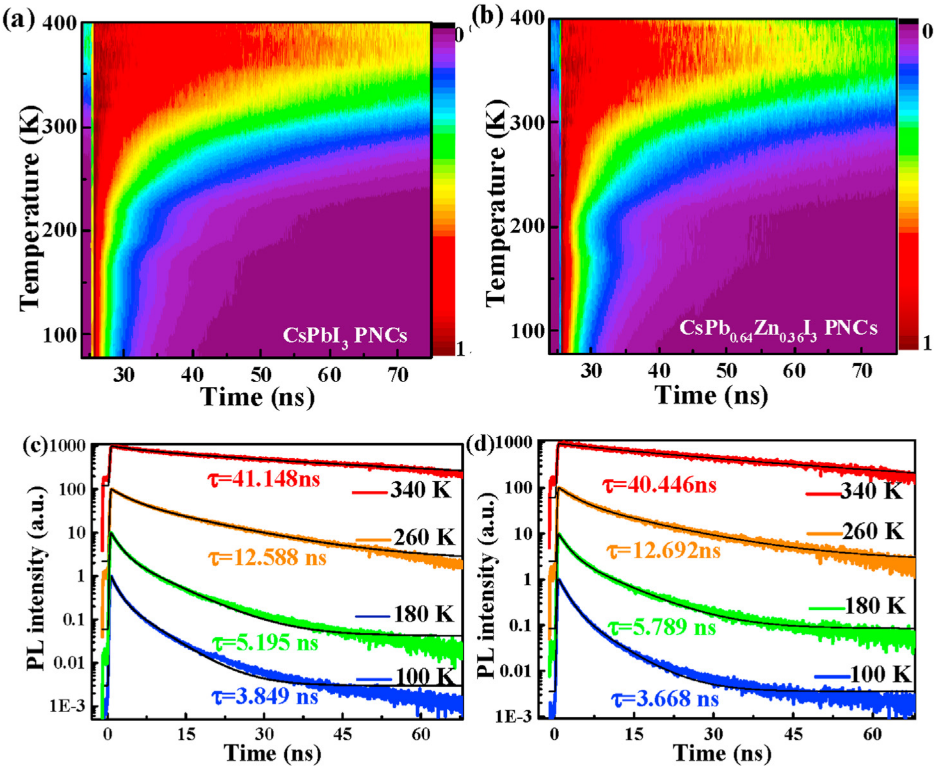

**Fig. 5.** 2D colors of TRPL dynamics for (a) $CsPbI_3$ PNCs and (b) $CsPb_{0.64}Zn_{0.36}I_3$ PNCs in different temperature. PL dynamics at various temperature for (c) $CsPbI_3$ PNCs and (d) $CsPb_{0.64}Zn_{0.36}I_3$ PNCs. (For interpretation of the references to color in this figure legend, the reader is referred to the Web version of this article.)

where $\tau_1$ and $\tau_2$ are the lifetimes of short and long-lived PL components, respectively. The biexponential decays strongly demonstrate two different species are involved in the exciton recombination. $A$ represents the baseline of PL while $B$ and $C$ represent the amplitudes of the whole normalized PL. The instrumental response function $\tau_{fwhm}$ is considered to convolute to PL decays. The average lifetimes ($\tau_{aver}$) can be calculated as,

$$\tau_{aver} = \left(B\tau_1^2 + C\tau_2^2\right) \Big/ (B\tau_1 + C\tau_2) \tag{4}$$

The above two processes dominate at high concentrations of PNCs or large size distribution of PNCs because the higher photon energy emitted by a smaller PNC will be re-absorbed by a larger PNC with a smaller optical bandgap, and/or the excited smaller PNC nonradiatively transfers its energy to a larger PNC. For evaluating the above processes occurring in pure $CsPbI_3$ and $CsPb_{0.64}Zn_{0.36}I_3$ PNCs, PL decays at different emission energies are carried out and displayed in Fig. S7.

Fig. 5 (a, b) show the lifetimes at varied temperatures for pure $CsPbI_3$ and $CsPb_{0.64}Zn_{0.36}I_3$ PNCs, the radiative and nonradiative decay rates ($k_r$ and $k_{nr}$) (see the Supporting Information) are calculated (see Table 1). The radiative decay rates increase 18-fold in $CsPb_{0.64}Zn_{0.36}I_3$ PNCs, the results indicate that the ultralow trap density for $CsPb_{0.64}Zn_{0.36}I_3$ PNCs. The average lifetimes change over the entire temperature range as shown in Fig. S8. It is noted that the PL lifetimes become longer at an elevated temperature as the temperature increases from 80 to 350 K for pure $CsPbI_3$ and $CsPb_{0.64}Zn_{0.36}I_3$ PNCs. For temperature below 250 K, there is no significant difference in lifetime between $CsPbI_3$ and $CsPb_{0.64}Zn_{0.36}I_3$ PNCs. It shows an initial increase in the lifetime, due to weak exciton-phonon (EP) interaction, so the radiative recombination of single exciton state dominates the carrier decay. Thus, at elevated temperatures, thermal motion becomes more active and thus prevents the recombination of exciton as shown in Fig. 5 (c). For temperature higher than 250 K, $CsPbI_3$ and $CsPb_{0.64}Zn_{0.36}I_3$ PNCs in lifetime begin to difference, the increasing EP interaction raises the probability of nonradiative recombination and reduces the PL lifetime [42]. The average PL lifetime of $CsPb_{0.64}Zn_{0.36}I_3$ PNCs is measured to be 18 ns, which is shorter than that of the pure $CsPbI_3$ PNCs (20 ns) from 250 to 350 K. Herein, the decrease in lifetime implies that the apparent increased radiative decay rates increased and nonradiative decay rates decreased when the Zn-to-(Zn+Pb) ratio increased from 0 to 0.36. The shortened PL lifetime indicates the presence of a new exciton relaxation pathway, namely energy transfer. The fast PL lifetime at the nanosecond scale suggest that the following energy transfer should complete in the nanosecond scale to survive severe PL quenching. Filling of conduction band with extra electrons provided by alloying usually results in PL enhancement, the impact of nonradiative trapping states on this PL channel is insignificant; otherwise, PL quenching would take place instead. Thus, it is safe to conclude that the zinc alloying induced near band-edge states are of radiative nature; in other words, they behave in a manner of providing more emissive channels rather than nonradiative trapping channels.

**Table 1**
PL decay parameters of pure and zinc alloyed $CsPbI_3$ PNCs.

| Sample | $\tau_1$/ns | $\tau_2$/ns | $\tau_{aver}$/ns | $k_r$/ns$^{-1}$ | $k_{nr}$/ns$^{-1}$ |
|---|---|---|---|---|---|
| $CsPbI_3$ PNCs | 5.224 | 32.702 | 30.522 | 0.0016 | 0.0312 |
| $CsPb_{0.64}Zn_{0.36}I_3$ PNCs | 4.854 | 22.845 | 21.100 | 0.0284 | 0.0189 |

### 3.5. *Transient absorption*

To reveal the mechanisms responsible for enhanced exciton recombination in zinc alloyed $CsPbI_3$ PNCs, TA technique is carried out to provide supplementary analysis on the carrier relaxation. Recently, comprehensive TA investigations on the exciton dynamics have been reported by using femtosecond TA and PL upconversion technique [50], in order to understand inorganic PNCs to determine the properties of charge carriers, their deactivation pathways and dynamics [43,44]. Fig. 6 (a, c) show the three-dimensional plot of TA spectra recorded from the CsPbI$_3$ and CsPb$_{0.64}$Zn$_{0.36}$I$_3$ PNCs. Fig. 6 (b, d) display the TA spectra at different pump probe delays time. Following the spectral analysis in a similar CsPbBr$_3$ system, we can readily attribute the spectral profiles of probe bleach (PB), to the ground-state bleach, and link those of photoinduced absorption (PA), labeled PA1 and PA2, to the lowest excitonic states and higher lying excitonic states, respectively. It is not hard to find that the kinetics of PA signal are almost identical to the PB signal for the two species, confirming that these signals are related to the carriers at the band edge. Compared with the pure one, it is obvious that the PB signal is broadened, which may be caused by the introduction of new energy level states. In both pure and alloyed cases, a redshift of the PB band in the time frame is observed, which is most likely due to the state filling of the initially generated hot exciton [45]. The bleach recovery dynamics of PNCs represents the dynamics of relaxation of the band-edge exciton, which is consist of three components. The first component is attributed to the cooling of the hot exciton ($\tau_1$) which is very fast. The second component ($\tau_2$) is often observed, which is assigned to carrier trapping. The long component ($\tau_3$) exists due to the electron-hole recombination process. Fig. 5 shows the temporal evolution of TA spectra (taken at several representative probe delays ranging from 0 ps to 1.2 ns) for CsPbI$_3$ and CsPb$_{0.64}$Zn$_{0.36}$I$_3$ PNCs, respectively. Generally, the excitation and recombination processes associated with exciton are simplified in Fig. 6 (f). Upon excitation by absorbing a high energy photon, an electron transits to the conduction band (purple arrow), which then decays to the band edge quickly and forms a free exciton (orange dashed arrows). The formed exciton is trapped by trapping states resulting from defects or alloying and exciton recombination. Given that the scan of probe delays is limited to ~1 ns in our TA measurements, so the relatively slow $\tau_3$ process can only be given by estimation (>1 ns). Because the $\tau_1$ process is very fast that the time scale is hundreds of femtoseconds or several picoseconds, the fitted short and long lifetimes can be assigned to trapping of exciton and band-edge exciton recombination processes [43]. Given the complex blending of these spectral profiles, a

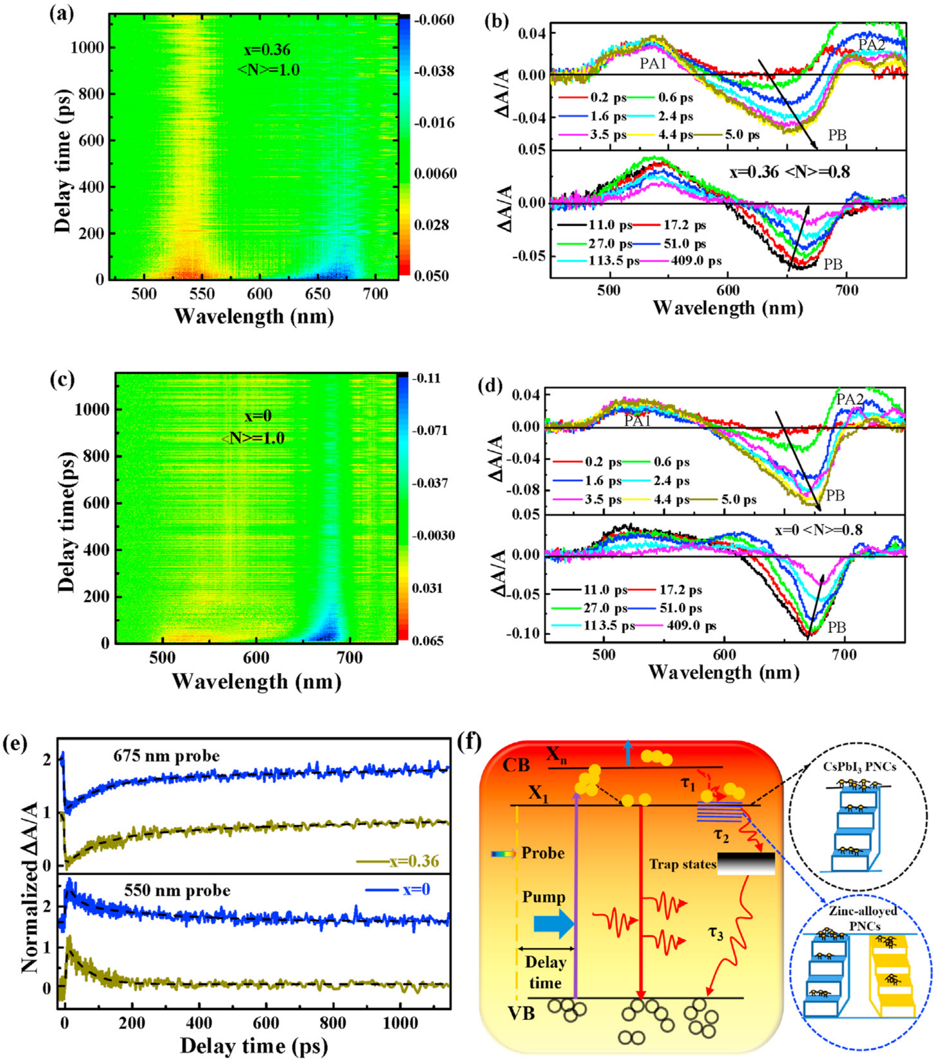

**Fig. 6.** 2D color maps of TA spectra of (a) CsPb$_{0.64}$Zn$_{0.36}$I$_3$ (c) CsPbI$_3$ PNCs, TA spectra at different probe delay times of (b) CsPb$_{0.64}$Zn$_{0.36}$I$_3$, (d) CsPbI$_3$ PNCs. (e) Bleach recovery dynamics of CsPb$_{0.64}$Zn$_{0.36}$I$_3$, CsPbI$_3$ PNCs at 675 nm of PB signal and at 550 nm of PA signal. (f) Schematic illustration of the TA involved photophysical processes, where VB, CB, X$_1$, X$_n$ denote valence band, conduction band, the lowest excitonic state in the CB, and the higher-lying excitonic states in the CB, respectively. (For interpretation of the references to color in this figure legend, the reader is referred to the Web version of this article.)

biexponential function is employed to obtain the characteristic decay associated spectra in Fig. 6 (e).

The corresponding time constants are extracted as follow: $\tau_2$=146.2 ps, $\tau_3$>1.00 ns for $CsPbI_3$ PNCs, while $\tau_2$=143.1 ps, $\tau_3$>1.00 ns for the $CsPb_{0.64}Zn_{0.36}I_3$ PNCs. $\tau_2$ and $\tau_3$ component as schematically illustrated by the two wiggly downward-pointing arrows (orange) in Fig. 6 (f). Apparently, the former process is faster in $CsPb_{0.64}Zn_{0.36}I_3$ PNCs than $CsPbI_3$ PNCs. As a result, the coupling between the Zn-induced lowest excited state and exciton trapping state is promoted, which accelerates the whole relaxation process and promotes the exciton recombination [46]. The effect can be understood as a result of the alloying-induced state modification. As the conduction band is formed mainly by the Pb orbitals, partial substitution of Pb with Zn is expected to change the distribution of energy levels in the conduction band. As is known, alloyed metal ions into the lattice of inorganic PNCs normally bring a new, near band-edge states [47], leading to an increased density of the lowest excitonic states that promoted the states coupling involved in the relaxation process. This increase in the density of states will promote the process like intraband hot-exciton relaxation as well as exciton trapping to the band-gap trapping states [48]. In other words, the new behavior of band edge states is to provide more channels to assist excitons in radiative recombination rather than non-radiative channels. Such metal ions can stabilize the $CsPbX_3$ surface and provide additional electronic states near the conduction band edge, thereby contributing to more emissive channels rather than non-radiative trapping centers. For high-level density functional theory (DFT) calculations, what we need to pay attention to here is alloying of metal ions can lead to PL enhancement band-edge states, they do not create any deep trapping states.

## 4. Conclusions

On all accounts, it is shown that one can dramatically enhance the PLQY of weakly emitting $CsPbI_3$ PNCs by using an appropriate quantity of $ZnI_2$ during temperature-pressure assisted crystallization approach. Temperature-dependent steady-state PL results indicate that higher exciton binding energy of zinc alloyed $CsPbI_3$ PNCs exhibit enhanced thermal stability compared with that of pure $CsPbI_3$ PNCs. A lower $\hbar\omega_{op}$ for $CsPbI_3$ PNCs implies that more optical phonons are produced, which would serve as a scattering center for nonradiative relaxation of excitons. We also measure the time-dependent TEM and spectroscopy of PNCs, and in so doing are to investigate the environmental thermal stability of zinc alloyed $CsPbI_3$ PNCs compared with $CsPbI_3$ PNCs. A higher structural stability and spectral stability indicate that cubic phase of zinc alloyed $CsPbI_3$ PNCs are more stable than $CsPbI_3$ PNCs. TRPL measurement and TA spectroscopy study reveals suppression of non-radiative carrier trapping centers and introduction of a new, near band-edge state facilitating radiative recombination process making these Zn alloyed PNCs brightly luminescent. The Pb substitution with Zn is partly achieved and effectively improve the PL enhancement and thermal stability of $CsPbI_3$ PNCs. The findings are likely to further enhance the potential of $CsPbI_3$ PNCs in optoelectronic applications.

## CRediT authorship contribution statement

**Ruirui Wu:** Data curation, Formal analysis, Writing - original draft, preparation. **Qi Wang:** Conceptualization, Software. **Sen Yang:** Methodology, Validation. **Lifang Wu:** Software, Validation. **Shunfa Gong:** Writing - review & editing. **Qiuju Han:** Writing - review & editing. **Wenzhi Wu:** Supervision, Funding acquisition.

## Declaration of competing interest

The authors declare that they have no known competing financial interests or personal relationships that could have appeared to influence the work reported in this paper.

## Acknowledgements

The authors are grateful for the support from scientific foundation of key project by Heilongjiang province (ZD2018014) and young scholar innovation team of Heilongjiang University (RCYJTD201901).

## Appendix A. Supplementary data

Supplementary data to this article can be found online at https://doi.org/10.1016/j.jallcom.2020.157574.

## References

[1] A. Dutta, N. Pradhan, Phase-stable red-emitting $CsPbI_3$ nanocrystals: successes and challenges, ACS Energy Letters 4 (2019) 709–719.
[2] M. Kulbak, D. Cahen, G. Hodes, How important is the organic part of lead halide perovskite photovoltaic cells? Efficient $CsPbBr_3$ cells, J. Phys. Chem. Lett. 6 (2015) 2452–2456.
[3] H. Wei, Y. Fang, P. Mulligan, W. Chuirazzi, H.-H. Fang, C. Wang, B.R. Ecker, Y. Gao, M.A. Loi, L. Cao, J. Huang, Sensitive X-ray detectors made of methylammonium lead tribromide perovskite single crystals, Nat. Photon. 10 (2016) 333–339.
[4] S. Yakunin, L. Protesescu, F. Krieg, M.I. Bodnarchuk, G. Nedelcu, M. Humer, G. De Luca, M. Fiebig, W. Heiss, M.V. Kovalenko, Low-threshold amplified spontaneous emission and lasing from colloidal nanocrystals of caesium lead halide perovskites, Nat. Commun. 6 (2015) 8056–8063.
[5] L. Zhang, Y. Liu, Z. Yang, S.F. Liu, Two dimensional metal halide perovskites: promising candidates for light-emitting diodes, Journal of Energy Chemistry 37 (2019) 97–110.
[6] A. Swarnkar, A.R. Marshall, E.M. Sanehira, B.D. Chernomordik, D.T. Moore, J.A. Christians, T. Chakrabarti, J.M. Luther, Quantum dot-induced phase stabilization of $\alpha$-$CsPbI_3$ perovskite for high-efficiency photovoltaics, Science 354 (2016) 92–95.
[7] M. Saliba, T. Matsui, J.-Y. Seo, K. Domanski, J.-P. Correa-Baena, M.K. Nazeeruddin, S.M. Zakeeruddin, W. Tress, A. Abate, A. Hagfeldt, Cesium-containing triple cation perovskite solar cells: improved stability, reproducibility and high efficiency, Energy Environ. Sci. 9 (2016) 1989–1997.
[8] C. Wang, A.S. Chesman, J.J. Jasieniak, Stabilizing the cubic perovskite phase of $CsPbI_3$ nanocrystals by using an alkyl phosphinic acid, Chem. Commun. 53 (2017) 232–235.
[9] B. Li, Y. Zhang, L. Fu, T. Yu, S. Zhou, L. Zhang, L. Yin, Surface passivation engineering strategy to fully-inorganic cubic $CsPbI_3$ perovskites for high-performance solar cells, Nat. Commun. 9 (2018) 1076–1083.
[10] S. Jeon, S.Y. Lee, S.-K. Kim, W. Kim, T. Park, J. Bang, J. Ahn, H.K. Woo, J.-Y. Chae, T. Paik, T.-Y. Seong, S.J. Oh, All-solution processed multicolor patterning technique of perovskite nanocrystal for color pixel array and flexible optoelectronic devices, Advanced Optical Materials 8 (2020) 2000501–2000509.
[11] X. Zhou, J. Jankowska, H. Dong, O.V. Prezhdo, Recent theoretical progress in the development of perovskite photovoltaic materials, Journal of Energy Chemistry 27 (2018) 637–649.
[12] D.P. Nenon, K. Pressler, J. Kang, B.A. Koscher, J.H. Olshansky, W.T. Osowiecki, M.A. Koc, L.-W. Wang, A.P. Alivisatos, Design principles for trap-free $CsPbX_3$ nanocrystals: enumerating and eliminating surface halide vacancies with softer lewis bases, J. Am. Chem. Soc. 140 (2018) 17760–17772.
[13] Y. Song, X. Zhang, L. Li, Z. Mo, J. Xu, S. Yu, X. Liu, J. Zhang, Temperature-dependent photoluminescence of cesium lead halide perovskite ($CsPbX_3$, X=Br, Cl, I) quantum dots, Mater. Res. Express 6 (2019) 115064–115072.
[14] C.J. Bartel, C. Sutton, B.R. Goldsmith, R. Ouyang, C.B. Musgrave, L.M. Ghiringhelli, M. Scheffler, New tolerance factor to predict the stability of perovskite oxides and halides, Science Advances 5 (2019) eaav0693-0701.
[15] F. Liu, C. Ding, Y. Zhang, T.S. Ripolles, T. Kamisaka, T. Toyoda, S. Hayase, T. Minemoto, K. Yoshino, S. Dai, M. Yanagida, H. Noguchi, Q. Shen, Colloidal synthesis of air-stable Alloyed $CsSn_{1-x}P_xI_3$ perovskite nanocrystals for use in solar cells, J. Am. Chem. Soc. 139 (2017) 16708–16719.
[16] Z. Zhang, L. Shen, H. Zhang, L. Ding, G. Shao, X. Liang, W. Xiang, Novel red-emitting $CsPb_{1-x}Ti_xI_3$ perovskite QDs@glasses with ambient stability for high efficiency white LEDs and plant growth LEDs, Chem. Eng. J. 378 (2019) 122125–122131.
[17] P.K. Nayak, M. Sendner, B. Wenger, Z. Wang, K. Sharma, A.J. Ramadan, R. Lovrinčić, A. Pucci, P.K. Madhu, H.J. Snaith, Impact of $Bi^{3+}$ heterovalent doping in organic–inorganic metal halide perovskite crystals, J. Am. Chem. Soc. 140 (2018) 574–577.

[18] A. Swarnkar, W.J. Mir, A. Nag, Can B-site doping or alloying improve thermal- and phase-stability of all-inorganic $CsPbX_3$ (X=Cl, Br, I) perovskites? ACS Energy Letters 3 (2018) 286–289.

[19] T.C. Jellicoe, J.M. Richter, H.F.J. Glass, M. Tabachnyk, R. Brady, S.E. Dutton, A. Rao, R.H. Friend, D. Credgington, N.C. Greenham, M.L. Böhm, Synthesis and optical properties of lead-free cesium tin halide perovskite nanocrystals, J. Am. Chem. Soc. 138 (2016) 2941–2944.

[20] M. Leng, Z. Chen, Y. Yang, Z. Li, K. Zeng, K. Li, G. Niu, Y. He, Q. Zhou, J. Tang, Lead-free, blue emitting bismuth halide perovskite quantum dots, Angew. Chem. Int. Ed. 55 (2016) 15012–15016.

[21] F. Li, Y. Liu, H. Wang, Q. Zhan, Q. Liu, Z. Xia, Postsynthetic surface trap removal of $CsPbX_3$ (X=Cl, Br, or I) quantum dots via a $ZnX_2$/hexane solution toward an enhanced luminescence quantum yield, Chem. Mater. 30 (2018) 8546–8554.

[22] M. Chen, Y. Zou, L. Wu, Q. Pan, D. Yang, H. Hu, Y. Tan, Q. Zhong, Y. Xu, H. Liu, B. Sun, Q. Zhang, Solvothermal synthesis of high-quality all-inorganic cesium lead halide perovskite nanocrystals: from nanocube to ultrathin nanowire, Adv. Funct. Mater. 27 (2017) 1701121–1701127.

[23] S. Zou, Y. Liu, J. Li, C. Liu, R. Feng, F. Jiang, Y. Li, J. Song, H. Zeng, M. Hong, X. Chen, Stabilizing cesium lead halide perovskite lattice through Mn(II) substitution for air-stable light-emitting diodes, J. Am. Chem. Soc. 139 (2017) 11443–11450.

[24] M. Que, Z. Dai, H. Yang, H. Zhu, Y. Zong, W. Que, N.P. Padture, Y. Zhou, O. Chen, Quantum-dot-induced cesium-rich surface imparts enhanced stability to formamidinium lead iodide perovskite solar cells, ACS Energy Letters 4 (2019) 1970–1975.

[25] Y. Dong, T. Qiao, D. Kim, D. Parobek, D. Rossi, D.H. Son, Precise control of quantum confinement in cesium lead halide perovskite quantum dots via thermodynamic equilibrium, Nano Lett. 18 (2018) 3716–3722.

[26] B. Conings, J. Drijkoningen, N. Gauquelin, A. Babayigit, J. D'Haen, L. D'Olieslaeger, A. Ethirajan, J. Verbeeck, J. Manca, E. Mosconi, F. De Angelis, H.-G. Boyen, Intrinsic thermal instability of methylammonium lead trihalide perovskite, Advanced Energy Materials 5 (2015) 1500477–1500484.

[27] K.-H. Wang, L.-C. Li, M. Shellaiah, K.W. Sun, Structural and photophysical properties of methylammonium lead tribromide ($MAPbBr_3$) single crystals, Sci. Rep. 7 (2017) 1–14.

[28] P.C. Sercel, J.L. Lyons, D. Wickramaratne, R. Vaxenburg, N. Bernstein, A.L. Efros, Exciton fine structure in perovskite nanocrystals, Nano Lett. 19 (2019) 4068–4077.

[29] Y. Liu, H. Lu, J. Niu, H. Zhang, S. Lou, C. Gao, Y. Zhan, X. Zhang, Q. Jin, L. Zheng, Temperature-dependent photoluminescence spectra and decay dynamics of $MAPbBr_3$ and $MAPbI_3$ thin films, AIP Adv. 8 (2018), 095108-095116.

[30] S.M. Lee, C.J. Moon, H. Lim, Y. Lee, M.Y. Choi, J. Bang, Temperature-dependent photoluminescence of cesium lead halide perovskite quantum dots: splitting of the photoluminescence peaks of $CsPbBr_3$ and $CsPb(Br/I)_3$ quantum dots at low temperature, J. Phys. Chem. C 121 (2017) 26054–26062.

[31] B.T. Diroll, H. Zhou, R.D. Schaller, Low-temperature absorption, photoluminescence, and lifetime of $CsPbX_3$ (X=Cl, Br, I) nanocrystals, Adv. Funct. Mater. 28 (2018) 1800945–1800951.

[32] J. Li, X. Yuan, P. Jing, J. Li, M. Wei, J. Hua, J. Zhao, L. Tian, Temperature-dependent photoluminescence of inorganic perovskite nanocrystal films, RSC Adv. 6 (2016) 78311–78316.

[33] M. Leng, Y. Yang, Z. Chen, W. Gao, J. Zhang, G. Niu, D. Li, H. Song, J. Zhang, S. Jin, J. Tang, Surface passivation of bismuth-based perovskite variant quantum dots to achieve efficient blue emission, Nano Lett. 18 (2018) 6076–6083.

[34] R. Li, S. Chen, X. Li, G. Yin, Y. Gong, J. Yu, G. Pang, J. Liu, Y. Liu, Z. Ni, L. Zhang, R. Chen, H.-L. Wang, Zn doped $MAPbBr_3$ single crystal with advanced structural and optical stability achieved by strain compensation, Nanoscale 12 (2020) 3692–3700.

[35] J. Lee, E.S. Koteles, M.O. Vassell, Luminescence linewidths of excitons in GaAs quantum wells below 150 K, Phys. Rev. B 33 (1986) 5512–5516.

[36] G. Morello, M. De Giorgi, S. Kudera, L. Manna, R. Cingolani, M. Anni, Temperature and size dependence of nonradiative relaxation and exciton-phonon coupling in colloidal CdTe quantum dots, J. Phys. Chem. C 111 (2007) 5846–5849.

[37] X. Shen, Y. Zhang, S.V. Kershaw, T. Li, C. Wang, X. Zhang, W. Wang, D. Li, Y. Wang, M. Lu, L. Zhang, C. Sun, D. Zhao, G. Qin, X. Bai, W.W. Yu, A.L. Rogach, Zn-alloyed $CsPbI_3$ nanocrystals for highly efficient perovskite light-emitting devices, Nano Lett. 19 (2019) 1552–1559.

[38] S. Yang, W. Fu, Z. Zhang, H. Chen, C.-Z. Li, Recent advances in perovskite solar cells: efficiency, stability and lead-free perovskite, J. Mater. Chem. A 5 (2017) 11462–11482.

[39] Q.A. Akkerman, S. Park, E. Radicchi, F. Nunzi, E. Mosconi, F. De Angelis, R. Brescia, P. Rastogi, M. Prato, L. Manna, Nearly monodisperse insulator $Cs_4PbX_6$ (X=Cl, Br, I) nanocrystals, their mixed halide compositions, and their transformation into $CsPbX_3$ nanocrystals, Nano Lett. 17 (2017) 1924–1930.

[40] Q. Wang, W. Wu, R. Wu, S. Yang, Y. Wang, J. Wang, Z. Chai, Q. Han, Improved thermal stability of photoluminescence in $Cs_4PbBr_6$ microcrystals/$CsPbBr_3$ nanocrystals, J. Colloid Interface Sci. 554 (2019) 133–141.

[42] K. Wei, Z. Xu, R. Chen, X. Zheng, X. Cheng, T. Jiang, Temperature-dependent excitonic photoluminescence excited by two-photon absorption in perovskite $CsPbBr_3$ quantum dots, Optic Lett. 41 (2016) 3821–3824.

[43] N. Mondal, A. Samanta, Complete ultrafast charge carrier dynamics in photo-excited all-inorganic perovskite nanocrystals ($CsPbX_3$), Nanoscale 9 (2017) 1878–1885.

[44] Y.-X. Zhang, H.-Y. Wang, Z.-Y. Zhang, Y. Zhang, C. Sun, Y.-Y. Yue, L. Wang, Q.-D. Chen, H.-B. Sun, Photoluminescence quenching of inorganic cesium lead halides perovskite quantum dots ($CsPbX_3$) by electron/hole acceptor, Phys. Chem. Chem. Phys. 19 (2017) 1920–1926.

[45] X. Huang, H. Li, C. Zhang, S. Tan, Z. Chen, L. Chen, Z. Lu, X. Wang, M. Xiao, Efficient plasmon-hot electron conversion in Ag-$CsPbBr_3$ hybrid nanocrystals, Nat. Commun. 10 (2019), 09112–09119.

[46] R. Cai, X. Qu, H. Liu, H. Yang, K. Wang, X.W. Sun, Perovskite light-emitting diodes based on $FAPb_{1-x}Sn_xBr_3$ nanocrystals synthesized at room temperature, IEEE Trans. Nanotechnol. 18 (2019) 1050–1056.

[47] R. Begum, M.R. Parida, A.L. Abdelhady, B. Murali, N.M. Alyami, G.H. Ahmed, M.N. Hedhili, O.M. Bakr, O.F. Mohammed, Engineering interfacial charge transfer in $CsPbBr_3$ perovskite nanocrystals by heterovalent doping, J. Am. Chem. Soc. 139 (2017) 731–737.

[48] J.-F. Liao, Y.-X. Chen, J.-H. Wei, Y.-T. Cai, X.-D. Wang, Y.-F. Xu, D.-B. Kuang, A facile method to fabricate high-quality perovskite nanocrystals based on single crystal powder, Nano Research 12 (2019) 2640–2645.

[49] W. Wu, W. Liu, Q. Wang, Q. Han, Q. Yang, Temperature-dependent photoluminescence of pure and Mn-doped $CsPbCl_3$ nanocrystals, Journal of Alloys and Compounds 787 (2019) 165–172.

[50] W. Wu, Y. Zhou, J. Wang, Y. Shao, D. Kong, Y. Gao, Y. Wang, The pump fluence and wavelength-dependent ultrafast carrier dynamics and optical nonlinear absorption in black phosphorus nanosheets, Nanophotonics 9 (2020) 2033–2043.